Composition-dependent photoluminescence properties and anti-counterfeiting applications of A_2AgX_3 (A = Rb, Cs; X= Cl, Br, I)

Pawan Kumar,[1†] Tielyr D. Creason,[1†] Hadiah Fattal,[1] Manila Sharma,[1] Mao-Hua Du,[2] Bayram Saparov[1]**

[1]Department of Chemistry and Biochemistry, University of Oklahoma, 101 Stephenson Parkway, Norman, OK 73019, United States

[2]Materials Science & Technology Division, Oak Ridge National Laboratory, Oak Ridge, Tennessee 37830, United States

*Corresponding authors: saparov@ou.edu; mhdu@ornl.gov
[†]These authors contributed equally

Abstract: All-inorganic copper(I) halides are emerging as attractive alternative materials to lead halide perovskites for optoelectronic and photonic applications. However, blue-emitting all-inorganic copper(I) halides suffer from poor stability and lack of tunability of their photoluminescence (PL) properties. Here, we report the preparation of silver(I) halides A_2AgX_3 (A = Rb, Cs; X= Cl, Br, I) through solid-state synthesis. In contrast to the Cu(I) analogs, A_2AgX_3 are tunable broad-band emitters sensitive to A and X site substitutions. First-principles calculations show that defect-bound excitons are responsible for the observed main PL peaks in Rb_2AgX_3 and the self-trapped exciton contributes to a minor PL peak in Rb_2AgBr_3. This is in sharp contrast to Rb_2CuX_3, in which the PL is dominated by the emission by self-trapped excitons. Moreover, the replacement of Cu(I) with Ag(I) in A_2AgX_3 significantly improves photostability and stability in air under ambient conditions, which enables their consideration for practical applications. Thus, luminescent inks based on A_2AgX_3 were prepared and successfully used in anti-counterfeiting

applications. The excellent light emission properties, significantly improved stability, simple preparation method, and tunable light emission properties demonstrated by A_2AgX_3 suggest that silver(I) halides may be attractive alternatives to toxic lead halide perovskites and unstable copper(I) halides for optical applications.

1. Introduction

In the past decade, multinary metal halides have been receiving increased attention due to their wide range of applications, including photodetectors, light-emitting diodes (LEDs), and solar cells.[1-10] Significant progress has recently been made to develop structurally unique metal halides to tune their functional properties for specific applications. Lead halides receive the most attention among various metal halides due to their outstanding photophysical properties, such as the low threshold for lasing, tunable band gaps, and photoluminescence (PL) in the entire visible spectral range, to name just a few.[3, 6, 11-14] Despite their excellent optical and electronic properties, the toxicity of lead and instability of lead halides in humid environments are among the significant concerns in this field.[6, 10] Therefore, considerable efforts have been devoted to developing alternative eco-friendly lead-free metal halides with improved stability.[7, 15-25] The initial focus for the replacement of Pb was on the same group elements, Sn and Ge, which yielded several exciting materials, but with much lower stability than the parent lead halides.[26, 27]

In recent years, the search for Pb-free alternatives was expanded to include halides of antimony (Sb), bismuth (Bi), and copper (Cu). The latter, Cu(I) halides, are interesting for optical applications.[7, 16-19, 23, 28-31] They combine many of the desirable attributes for practical applications such as eco-friendly, earth-abundant and inexpensive elemental compositions, simple processing, and high-efficiency light emission with photoluminescence quantum yield (PLQY) values approaching unity. The most prominent members of these recently discovered Cu(I) halide light emitters include $Cs_3Cu_2(Br,I)_5$, Rb_2CuX_3, and K_2CuX_3 (X = Cl, Br), which demonstrate near-unity PLQY blue emission at room temperature.[7, 18, 23, 29] Interestingly, as is evident from this list, the light emission properties of Cu(I) halides are very weakly dependent on the alkali metal and halogen sites, and therefore, their substitutions do not provide a route for tuning their PL emission.

This observation is in stark contrast to the all-inorganic lead halides such as the $CsPbX_3$, for which the wide range tunability of their PL emission is one of their noted advantages.[2, 3, 32, 33] The reason for the notably low tunability of PL properties of Cu(I) halides lies in the intricacies of their band structures: the top of the valence band and the bottom of the conduction band are dominated by Cu 3*d* and 4*s* orbitals, respectively.[34] Therefore, to change band structures and consequently light emission properties of copper(I) halides, a strategy can be formulated centered around the replacement of Cu(I) with a different metal such as Ag(I). Such substitution is also expected to improve the stability of Cu(I) halides, which is currently one of the significant barriers for considerations of Cu(I) halides for practical applications as materials such as Rb_2CuX_3 have been shown to degrade in humid air rapidly.[7] In contrast, the monovalent oxidation state is preferred by silver, and therefore, degradation via oxidation is unlikely to occur in Ag(I) halides.

The recently discovered ternary Cu(I) halides have been explored for varieties of applications such as in high-efficiency LEDs, fast scintillation and dynamic X-ray imaging.[7, 35, 36] In addition, highly luminescent materials can also be candidates for anti-counterfeiting applications due to their chemical durability, unique optical properties, low cost, difficulty in their duplications, and good concealment.[37] Estimated economic losses reached $1.7 trillion in 2015 due to counterfeiting, and this value has been increasing.[38] Various luminescent materials, including quantum dots, organic dyes, metal-organic frameworks (MOFs), lanthanide-based materials, and lead halides, have been tested for anti-counterfeiting applications.[37, 38] Here, we report a facile method of preparation of a new family of candidate materials for anti-counterfeiting applications – A_2AgX_3 (A= Rb, Cs; X= Cl, Br, I), which are substitution analogs of brightly luminescent blue-emitting A_2CuX_3. Confirming our materials design ideas, the replacement of Cu(I) with Ag(I) has a significant impact on the electronic band structures, and consequently, the light emission properties of

A_2AgX_3. Furthermore, we report a strategy for fabricating luminescent inks based on A_2AgX_3, which are used for high-end anti-counterfeiting labels with demonstrated stability in water, under heating and ultrasonication. The obtained materials were characterized using X-ray diffraction (PXRD) and optical spectroscopy methods. Our experimental work is complemented by comprehensive density functional theory (DFT) calculations, which suggest the much more significant contribution of halogen-*p* orbitals in the valence band of A_2AgX_3, as well as composition-dependent multi-excitonic emission including emissions from defect-bound excitons (DBEs) and self-trapped excitons (STEs), explaining the observed more tunable and starkly different PL properties. Our combined experimental and computational work shows that Ag(I) halides are an exciting new class of highly luminescent multinary halides with improved stability.

2. Results and Discussion

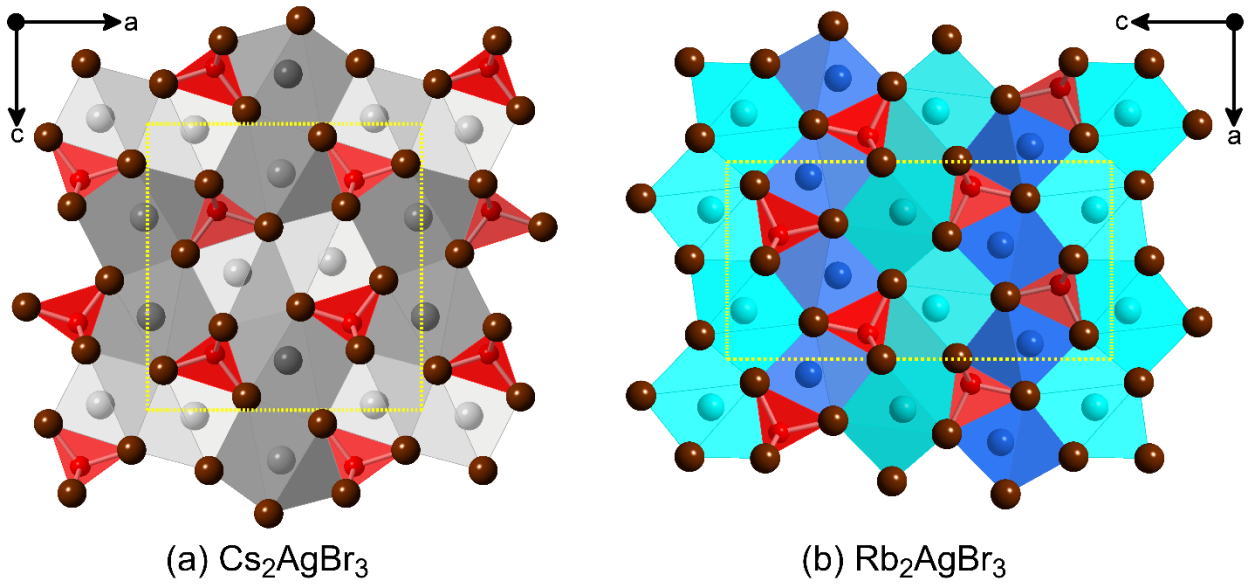

Figure 1. Orthorhombic crystal structures of (a) Cs_2AgBr_3 and (b) Rb_2AgBr_3 viewed down the *b*-axes Both compounds feature 1D $^1_\infty[AgX_3]^{2-}$ chains (shown in red) separated by A^+ cations. The difference in the packing of the $^1_\infty[AgX_3]^{2-}$ chains and A^+ cations is emphasized by displaying (a) Cs1 and Cs2 in dark grey and light grey in Cs_2AgBr_3 and (b) Rb1 and Rb2 in dark blue and light blue in Rb_2AgBr_3; Ag and Br are shown in red and brown, respectively.

A_2AgX_3 crystallize in the orthorhombic space group *Pnma* featuring 1D $^1_\infty[AgX_3]^{2-}$ chains separated by A^+ cations (Figure 1). In this family, the use of the larger Cs^+ cation results in the K_2CuCl_3 type structure, i.e., Cs_2AgX_3 are isostructural to A_2CuX_3. In contrast, the $^1_\infty[AgX_3]^{2-}$ chains are packed differently with respect to the A^+ cations in the case of the K_2AgI_3 type compounds Rb_2AgX_3 and K_2AgX_3 featuring the smaller alkali cations Rb^+ and K^+ (Figure 1).

To determine the bulk purity and environmental stability of the as prepared A_2AgX_3 samples, periodic PXRD measurements were taken over four weeks at room temperature. This data was then fitted to the previously published structures of these compounds to ensure excellent purity.[39] The room temperature PXRD patterns of A_2AgX_3 are illustrated in Figure S1 (a-e). Our PXRD results suggest that the preparation method employed in this work is an effective route for syntheses of high purity and high crystallinity A_2AgX_3 materials. Furthermore, Rb_2AgX_3 are found to have significantly improved air stability with no measurable changes for the samples left in ambient air for four weeks (Figures S2). This contrasts with the reported poor stability of Rb_2CuX_3 (X= Cl, Br), which show noticeable degradation in days and are largely degraded in bulk within a month.[7]

Moreover, the thermal stability of Rb_2AgCl_3, Rb_2AgBr_3, and Rb_2AgI_3 was also evaluated by heating polycrystalline powder samples at 100 °C for 48 hours, which suggests that these compounds are structurally stable under these conditions (Figures S3). Thermogravimetric analysis (TGA) measurements suggest that A_2AgX_3 show no significant loss in weight up to 450 °C (Figure S4). This observation is consistent with the improved thermal stability of all-inorganic metal halides such as Rb_2CuX_3, $Rb_4Ag_2BiBr_9$, $Cs_3Cu_2Br_{5-x}I_x$, and Cs_2SnI_6 as compared to hybrid organic-inorganic metal halides.[7, 20, 23, 26, 29] The differential scanning calorimetry (DSC) results demonstrate that Rb_2AgCl_3, Rb_2AgBr_3, Rb_2AgI_3, Cs_2AgBr_3, and Cs_2AgI_3 show peritectic

decompositions at 303.4 °C, 296.9 °C, 303.4 °C, 297.4 °C, 257.9 °C, and 252.8 °C, respectively, which matches with the reported phase diagram for compounds that were previously studied (Figure S4).[40, 41]

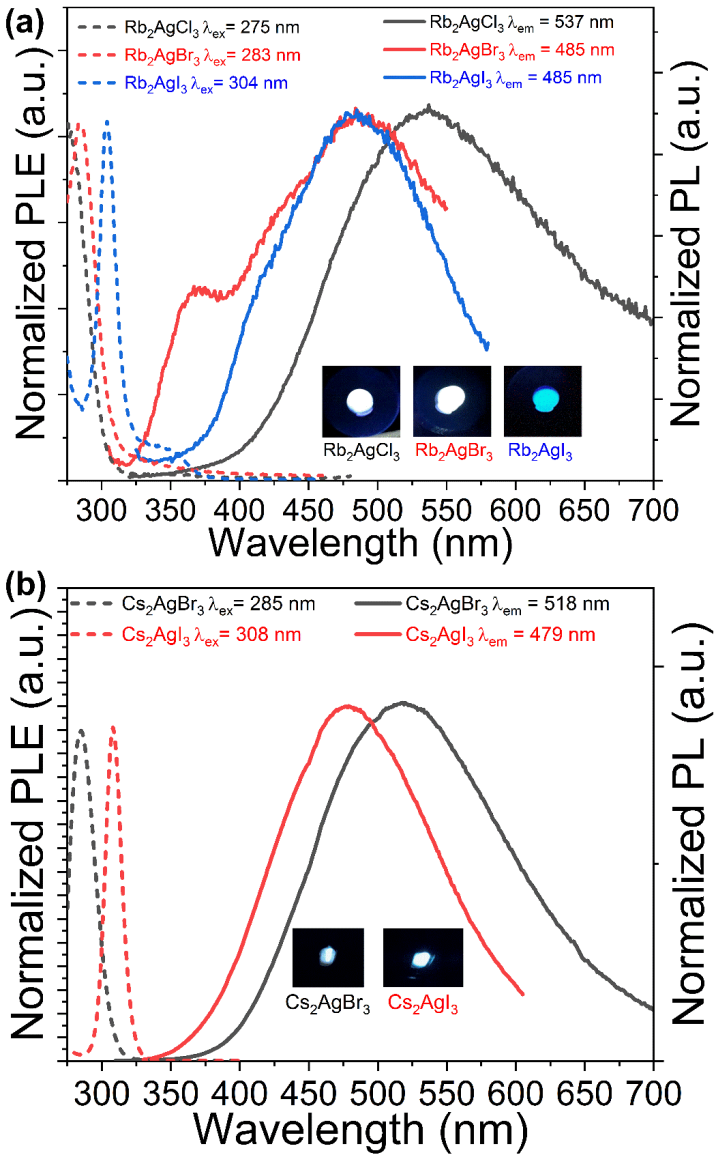

Figure 2. Normalized room temperature photoluminescence excitation (PLE) and photoluminescence emission (PL) plots for (a) Rb_2AgX_3 and (b) Cs_2AgX_3. Insets show the visible emission from samples when excited with their respective excitation maxima.

Photoluminescence excitation (PLE) and emission (PL) spectra of A_2AgX_3 are provided in Figure 2. PLE spectra of Rb_2AgCl_3, Rb_2AgBr_3, Rb_2AgI_3, Cs_2AgBr_3, and Cs_2AgI_3 show sharp excitation bands centered at 280 nm, 284 nm, 304 nm, 285 nm, and 308 nm, respectively, which give broad emission peaks with maxima at 534 nm, 484 nm, 483 nm, 518nm, and 479 nm, respectively. The obtained PLE spectra are strikingly similar to that of A_2CuX_3, with PLE maxima at virtually the same wavelength.[7, 17-19] In contrast, the PL emission spectra are both significantly red-shifted and have a larger full width at half-maximum (FWHM) than the A_2CuX_3 counterparts.[7, 17-19] This broadband emission causes the A_2AgX_3 compounds to have a white or bluish-white emission compared to Cu(I) analogs A_2CuX_3, which are all blue emitters.[18, 19, 34] Based on our PL and PLE results, Rb_2AgCl_3, Rb_2AgBr_3, Rb_2AgI_3, Cs_2AgBr_3, and Cs_2AgI_3 exhibit large Stokes shift values of 254 nm, 200 nm, 179 nm, 233 nm, and 171 nm, respectively. The observed large Stokes shifts in low-dimensional metal halides are typically a sign of light emission originating from self-trapped excitons (STEs) and defect-bound excitons (DBEs).[17, 19, 28, 34, 42-44] Notably, the large Stokes shift values for A_2AgX_3 are approximately double of what is observed in the A_2CuX_3 compounds, which is explained below by the difference in the main emission mechanisms, i.e., the DBE emission in A_2AgX_3 vs. the STE emission in A_2CuX_3. .[7, 18, 34] This observation is also consistent with the previous work on doped NaF samples, which also showed a stronger lattice coupling for Ag^+ compared Cu^+ doping.[45]

The measured PL properties of A_2AgX_3 show tunability through substitution including some changes with substitutions on the A^+ cation site and more pronounced changes via the substitutions on the halide site. The composition dependence of PL in A_2AgX_3 is in stark contrast with the nearly complete lack of tunability observed for the analogous blue-emitting Rb_2CuX_3 and K_2CuX_3.[34] The weak tunability of PL properties of A_2CuX_3 has been explained by the fact that the Cu states

dominate the states around the band gap and that the STEs formed in these compounds are localized around the Cu sites.[7, 18, 34] In comparison, our results on A_2AgX_3 suggest that defects play a more significant role in their PL properties. We find that certain members of this system exhibit both DBEs and STEs (see the computational analysis section below), which in combination provide broader and more tunable light emission properties.

To better understand the light emission properties of A_2AgX_3, excitation wavelength-dependent PL spectra (Figure S5) were measured. Most notable changes occur for Rb_2AgI_3, in which higher excitation energy causes a small red shift in the PL emission. Other members of the A_2AgX_3 have largely preserved PL peak shapes and positions. In addition, we performed PLE measurements for a variety of emission wavelengths, which confirmed that the observed PL emission peaks were all related to a singular PLE maximum in each of the compounds (Figure S6). These measurements reveal that in each of A_2AgX_3, a single photoexcited state is the source of their respective PL emission spectra, including the case of Rb_2AgBr_3, which clearly shows the presence of multiple emission centers (Figure 2). The case of Rb_2AgBr_3 is particularly interesting because its measured photophysical properties indicate the presence of two emission centers, which are assigned to DBE and STE centers (see below). In combination with the observed large Stokes shifts and broad emission spectra, our in-depth PL results are suggestive of primarily defect-bound exciton emission in A_2AgX_3.

The lifetime of PL emission from any luminescent material is an essential parameter for the potential practical applications of luminescent materials. For example, for certain photodetector and sensing applications, luminescent materials with faster decay rates are more desirable, while luminescent materials with longer decay are more suitable for signal or self-luminous light source applications.[46, 47] For A_2AgX_3, the TRPL decay profiles and their exponential fits are provided in

Figures S7; the decay profiles were fitted with double-exponential function as where τ_1 and τ_2 are the decay lifetimes of the luminescence, and A1 and A2 are the weighting parameters. The fitting results of our TRPL data are provided in Table S1. The observed average lifetime of Rb_2AgCl_3, Rb_2AgBr_3, Rb_2AgI_3, Cs_2AgBr_3, and Cs_2AgI_3 polycrystalline powders are 0.62 μsec, 0.77 μsec,1.15 μsec, 58.82 μsec, and 14.67 μsec, respectively. These lifetimes are on par with the ~10-12 μsec lifetimes reported in A_2CuX_3 compounds, which have triplet-STE-based emission, suggesting a similar triplet-exciton-based light emission in A_2AgX_3. In contrast, free exciton emission is characterized by significantly faster emission on the nanosecond scale.[48, 49]

Electronic band structures and DOS of Rb_2AgX_3 (X = Cl, Br, I) obtained by PBE calculations are shown in Figure 3. The band gap of Rb_2AgCl_3 is direct at the Γ point, while those of Rb_2AgBr_3 and Rb_2AgI_3 are slightly indirect. The conduction band minima (CBM) of both Rb_2AgBr_3 and Rb_2AgI_3 are located at the Γ point, while their valence band maxima (VBM) at the X point are slightly higher than those at the Γ point by 0.01 eV. The direct band gaps of all three halides calculated using both the PBE and hybrid PBE0 functionals are shown in Table S2.

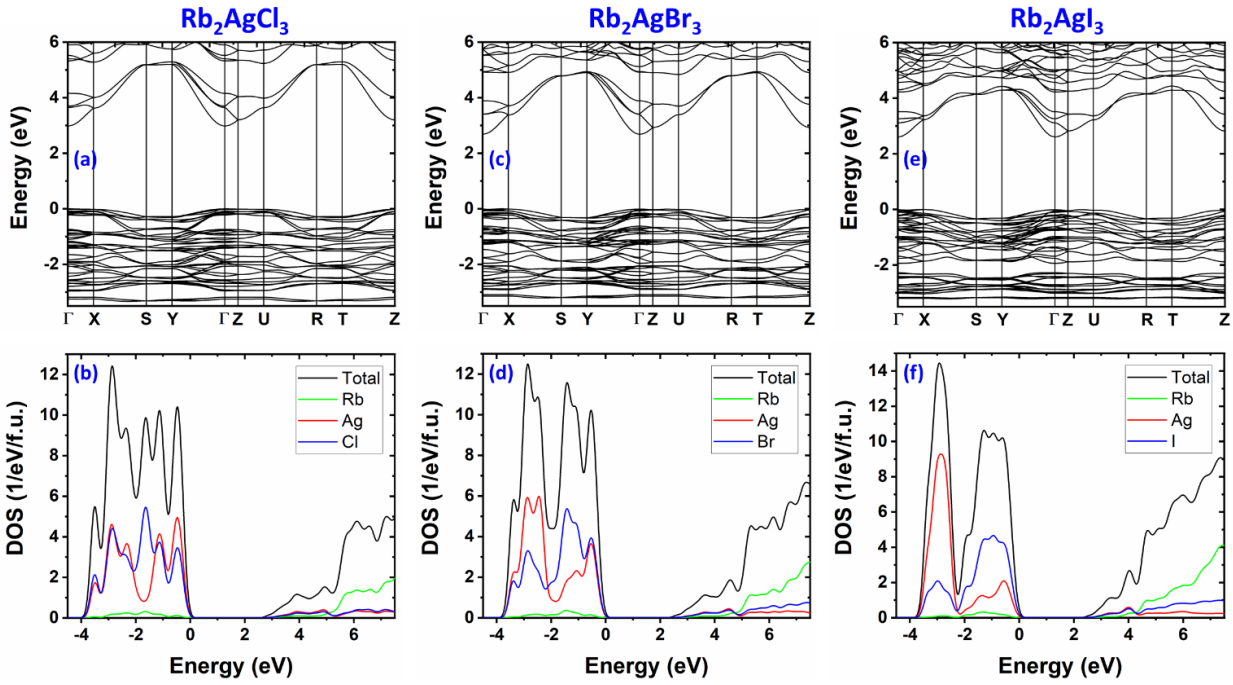

Figure 3. Electronic band structure and density of states (DOS) of Rb_2AgCl_3 (a-b), Rb_2AgBr_3 (c-d), and Rb_2AgI_3 (e-f), respectively.

Figure 3 shows that the conduction band of Rb_2AgX_3 is made up of Ag-5*s* orbitals, which hybridize with halogen-*p* orbitals, while the valence band is a mixing of Ag-4*d* and halogen-*p* states. The band gaps follow the normal decreasing trend from Rb_2AgCl_3, Rb_2AgBr_3, to Rb_2AgI_3, consistent with the red shift of excitation energies observed in the experiments. This is in contrast to Rb_2CuX_3 and K_2CuX_3, in which Cu-3*d* orbitals dominate the valence band, and thus the band gap is nearly independent on the type of the halogen ion.

Table 1. Calculated STE excitation and emission energies.

Rb_2AgCl_3		Rb_2AgBr_3		Rb_2AgI_3	
Excitation	Emission	Excitation	Emission	Excitation	Emission
4.821 eV (257 nm)	3.842 eV (323 nm)	4.436 eV (280 nm)	3.692 eV (336 nm)	4.203 eV (295 nm)	3.222 eV (385 nm)

To better understand the multi-excitonic nature of light emission in this family, calculations of excitonic properties were carried out for Rb_2AgX_3 (Tables 1-2). The calculated exciton excitation energies in Rb_2AgX_3 (X = Cl, Br, I) are 4.821 eV, 4.436 eV, and 4.203 eV, in good agreement with the experimentally observed values of 4.509 eV, 4.381 eV, and 4.078 eV, respectively. The strong excited-state structural relaxation (similar to that reported in Rb_2CuX_3) leads to the formation of a STE.[7] The calculated STE emission energies of 3.842 eV, 3.692 eV, 3.222 eV in Rb_2AgX_3 (X = Cl, Br, I) are much higher in energy than the main PL peaks of 2.309 eV, 2.556 eV, 2.556 eV, respectively (Table 1). Previous calculations utilizing the same computational method showed that calculated STE emission energies in low-dimensional halides agree well with PL peak energies with errors typically less than 0.3 eV.[50] The large differences between calculated STE emission energies and the observed main PL peak energies suggest that the main PL peaks in Figure 2(a) are likely due to other sources, such as native defects. We further investigated excitons trapped by vacancies (V_{Rb}^{-}, V_{Ag}^{-}, and V_{X}^{+}), which are typically the main defects in halides. There are three inequivalent halogen X sites, two inequivalent Rb sites, and one Ag sites in Rb_2AgX_3, which are shown in Figure S8. The calculated DBE emission energies are shown in Table 2; a comparison of calculated and experimental transition energy levels for Rb_2AgX_3 is provided in Figure S9. The calculated emission energies of excitons trapped by the most stable halogen vacancy (V_{X3}^{+}) are 2.477 eV in Rb_2AgCl_3 and 2.322 eV in Rb_2AgBr_3, which are in good agreement with the observed main PL peaks at 2.309 eV and 2.556 eV in the two respective compounds. For Rb_2AgI_3, the calculated emission energies of V_{Ag}^{-} (2.919 eV) and V_{Rb2}^{-} (2.935 eV) are reasonably close to the observed main PL peak at 2.556 eV. Therefore, we tentatively assign the main PL peaks in Rb_2AgCl_3 and Rb_2AgBr_3 to the halogen vacancy and that in Rb_2AgI_3 to cation vacancies. In

addition, the metastable halogen vacancy (V_{X2}^{+} in Rb_2AgCl_3 and Rb_2AgBr_3) could also contribute to the broad PL peak because its energy is just slightly higher than the most stable halogen vacancy. There is also a minor peak at 3.416 eV (363 nm) in the PL spectrum of Rb_2AgBr_3 (Figure S10), which is close to the calculated STE emission energy of 3.692 eV (336 nm). This suggests that some (but not all) excitation energy in Rb_2AgBr_3 is transferred from the triplet STE to defects, leading to emission by both STEs and defects, while, in Rb_2AgCl_3 and Rb_2AgI_3, STEs are likely quickly trapped by defects, resulting in the quenching of the STE emission. The observation of significant contributions of both STE and DBE to the PL of Rb_2AgBr_3 suggests that the timescale of STE trapping by defects is competitive to the STE emission time; therefore, it is reasonable to expect that the DBE emission time is comparable to even longer than the STE emission time, which is consistent with the measured long lifetimes of PL emission. The dual band emission mechanism in Rb_2AgBr_3 is responsible for its unusual white light emission.

The presence of halogen vacancy defects in ternary silver halides has been known and reported in the literature.[43, 51] Previously, the PL peak observed in Rb_2AgBr_3 was assigned to neutral V_{Br} (V_{Br1}^{0}) rather than V_{Br3}^{+} proposed in this work.[43] Note that the cation and anion vacancies in a large-gap halide are usually ionized and compensate each other, resulting in charge neutrality. At the +1 charge state, V_{Br1}^{+} is less stable than V_{Br3}^{+} and the calculated emission energy of V_{Br1}^{+} is much lower than the observed main PL peak, as shown in Table 2. On the other hand, our calculated band gap (5.10 eV) and STE emission energy (3.692 eV) in Rb_2AgBr_3 are in excellent agreement with those reported previously (5.1 eV and 3.7 eV).[43] This emission mechanism is also supported by the literature precedent of analogous ternary silver halides.[52]

As another supporting evidence for the significant role of defects in determining the photophysical properties of A_2AgX_3, previously it was reported that the pulling of vacuum on a

Rb_2AgBr_3 sample significantly increases the intensity of the defect PL peak.[43] To test this further, we prepared Rb_2AgI_3 using two differing techniques: (i) the more reliable method of sample preparation involved annealing of the sample in a vacuum sealed ampoule under 5 mTorr for 80 hours, followed by regrinding and reannealing for another 80 hours. The second method involved only a short annealing time of 12 hours. The PL spectra for resultant samples are starkly different (Figure S11), suggesting the dominant STE emission for the second sample with short annealing time. The emission energy for this sample matches well with the calculated STE transition energy (Figure S9 and Table 1). In contrast, the longer annealing produces a sample with a predominant DBE emission. However, we note that the STE/DBE intensity ratio significantly varies from sample to sample.

Table 2. Calculated emission energies from vacancies and STE. The energy of the lowest-energy exciton localized on the halogen/rubidium vacancy site is set to zero.

	Rb_2AgCl_3		Rb_2AgBr_3		Rb_2AgI_3	
	Energy (meV)	Emission	Energy (meV)	Emission	Energy (meV)	Emission
V_{X1}^{+}	134	0.712 eV (1742 nm)	214	1.325 (936 nm)	156	1.15011 (1078 nm)
V_{X2}^{+}	4	2.582 eV (480 nm)	42	2.433 eV (510 nm)	56	2.197 eV (564 nm)
V_{X3}^{+}	0	2.477 eV (501 nm)	0	2.322 eV (534 nm)	0	1.995 eV (621 nm)
V_{Rb1}^{-}	34	3.630 eV (342 nm)	90	3.453 eV (359 nm)	167	2.104 eV (589 nm)
V_{Rb2}^{-}	0	3.665 eV (338 nm)	0	3.520 eV (352 nm)	0	2.935 eV (422 nm)
V_{Ag}^{-}	N/A	3.782 eV (328 nm)	N/A	3.580 eV (346 nm)	N/A	2.919 eV (425 nm)
STE	N/A	3.842 eV (323 nm)	N/A	3.692 eV (336 nm)	N/A	3.222 eV (385 nm)
Exp. emission		2.309 eV (537 nm)		2.556 eV (485 nm)		2.556 eV (485 nm)

Advantageously, Pb-free all-inorganic A_2AgX_3 not only demonstrate improved air- and thermal-stability as compared to many of the known lead halide perovskites and analogous copper(I) halides, but also show visibly bright room-temperature light emission properties. The estimated PLQY values for fresh samples were 1.52%, 0.37%, 6.37% and 14.41% for Rb_2AgBr_3, Rb_2AgI_3, Cs_2AgBr_3 and Cs_2AgI_3, respectively. Note that these are conservative estimates since A_2AgX_3 are broadband emitters and our PLQY measurement ranges are constrained by the

excitation energy and its overtones. This is especially the case for the Rb_2AgX_3 species, including Rb_2AgCl_3, for which PLQY cannot be accurately estimated due to its high excitation energy. It is also previously reported that solid-state grown samples often significantly under report the PLQY when compared to single crystals.[7] Finally, a major difference between Ag(I) and Cu(I) halides is that in the former, defects play a lot more significant role in their photophysical behaviors. Therefore, the lower lying defect bands could also be routes for nonradiative recombination in this system. Notwithstanding the lower PLQYs of Ag(I) halides, A_2AgX_3 are also found to have improved photostability (Figure S12). Thus, under a continuous UV irradiation, Cs_2AgX_3 display only a small (< 8%) drop in PLQY values, indicating a significant improvement in photostability as compared to Cu(I) analogs such as Rb_2CuCl_3.[7] As for Rb_2AgX_3, the recorded increase in PLQY is due to both increased relative error of low PLQY of these compounds and formation of defects under continuous irradiation.

Figure 4. The words **"Saparov Lab"** were written on black paper using the fabricated luminescent ink based on A_2AgX_3 under normal light and UV light (365 nm).

Much improved environmental stability and PL tunability of A_2AgX_3 allows their consideration for practical uses such as anti-counterfeiting. The counterfeiting and duplicity of valuable documents such as diplomas, certificates, and currency are a rising critical problem worldwide. Recently, lead-based metal halides have been used for anti-counterfeiting applications, however,

the presence of toxic lead remains a major issue.[37, 38] We prepared luminescent inks to validate the feasibility of the as-prepared A_2AgX_3 for anti-counterfeiting applications. The fabricated inks contain A_2AgX_3 individual particles with sizes ranging from approximately 500 nm to a micron and much larger micron scale aggregates (Figure S13). For the proof of concept, the words **"Saparov Lab"** were printed on black paper using the fabricated luminescent ink based on A_2AgX_3 (Figure 4). Interestingly, all five members of A_2AgX_3 show unique emission colors, creating a possibility of multicolor patterns. Furthermore, to demonstrate the versatility of A_2AgX_3 based luminescent inks, we prepared prints on a variety of surfaces and colors, including white weighing papers (Figure S14), colored papers (Figure S15a), and transparent polyethylene bags, which can be utilized for commercial packing (Figure S16). In all cases, clearly discernible prints are observed under UV excitation. Our results reveal that the color of the printing surfaces does not affect the printed code words. Therefore, the A_2AgX_3 luminescent inks reported in this work can be used on any color surface, which is a significant advantage over other reported materials for anti-counterfeiting applications.

For potential practical applications of the A_2AgX_3 inks, the printed patterns' stability and durability are of the highest importance. The results suggest that the printed patterns using the A_2AgX_3 inks are water stable (Figure S17). Moreover, only a minimal luminescence intensity loss is observed under heating at elevated temperatures of 60 °C and 80 °C (Figure S14b). The mechanical stability of printed patterns was also tested by ultrasonication for 30 minutes at 25 kHz (Figure S18). The printed patterns on transparent polyethylene bags did not disappear entirely even after ultrasonication in water, which is a testament to the remarkable durability of the A_2AgX_3 based inks.

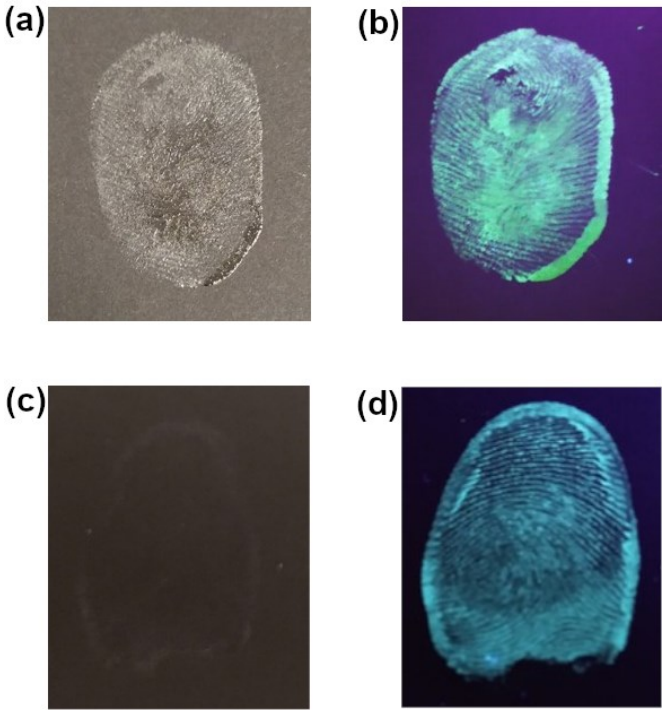

Figure 5. The A_2AgX_3 based luminescent inks can be used for fingerprints (FPs): (a, b) a print of a right thumb using Rb_2AgI_3 and (c, d) a print of a left thumb using Cs_2AgI_3 under normal light (a, c) and UV light (365 nm, b, d).

Fingerprints (FPs) and latent fingerprints (LFPs) are commonly used for medical diagnosis, national security and policing, control of access, and forensic investigations.[53] However, metal halide-based light emitters are underexplored for LFPs. Consequently, in addition to the anti-counterfeiting application of A_2AgX_3 based luminescent ink, we also explored their potential use in LFPs. The LFPs based Rb_2AgI_3 (right thumb) and Cs_2AgI_3 (left thumb) based luminescent inks were deposited on black paper. The deposited thumb impression is visible in normal light and shows bright fluorescence emission in UV light, which can be early observed and identified (Figure 5).

In summary, our results suggest that the A_2AgX_3 based luminescent inks are viable candidates for advanced LFPs and anti-counterfeiting applications. The A_2AgX_3 inks are versatile and can be

printed on any surface with any color background, including polyethylene surfaces. The possibility of printing A_2AgX_3-based patterns on polyethylene surfaces with high water and mechanical stability is particularly noted and can pave the way for applying these and related metal halides for commercial use.

3. Conclusion

We report a facile method of preparation of A_2AgX_3 (A = Rb, Cs; X= Cl, Br), which exhibit broadband PL emission spectra attributed to vacancy-bound excitons (DBEs) and in the case of Rb_2AgBr_3 STEs as well. A_2AgX_3 demonstrate markedly improved photo-, air- and thermal-stability compared to the high efficiency blue emitting Cu(I) analogs A_2CuX_3. Moreover, the measured optical properties show that PL emission properties of A_2AgX_3 are sensitive to A and X site substitutions, which is in stark contrast to the notable lack of tunability of PL properties of A_2CuX_3. The computational investigations reveal that the PL in Rb_2AgX_3 (X = Cl, Br, I) are dominated by the emission by vacancy-bound excitons with a minor contribution from the STE in the case of Rb_2AgBr_3 and the experimentally observed halogen dependence of the PL properties can be explained by the different type of defects involved in light emission. Tunability of PL properties of A_2AgX_3 and their much-improved stability allows their consideration for practical applications, which is demonstrated in this work by the preparation of A_2AgX_3 based luminescent inks for fingerprint detection and anti-counterfeiting applications. Our printed security patterns using the A_2AgX_3 inks are stable in water, under heat, and ultrasonication, further confirming the stability of A_2AgX_3. In combination, lead-free and earth-abundant elemental compositions, simple processing, high-efficiency tunable light emission, and improved environmental stability of A_2AgX_3 makes them attractive alternatives to toxic lead halide perovskites and unstable copper(I) halides for practical applications.

4. Experimental

Materials: Rubidium chloride (99%, Alfa Aesar), rubidium bromide (99%, Alfa Aesar), rubidium iodide (99%, Alfa Aesar), cesium bromide (>99%, Sigma-Aldrich), cesium iodide (>99%, Sigma-Aldrich), silver chloride (>99%, Alfa Aesar), silver bromide (99.5%, Alfa Aesar),silver iodide (99.999%, Alfa Aesar), polymethyl methacrylate (PMMA) (Sigma-Aldrich), and toluene (>99.5%, Sigma-Aldrich) were purchased and used as received.

Rb_2AgX_3 (X = Cl, Br, I) Synthesis: Rb_2AgX_3 (X = Cl, Br, I) were synthesized by a facile solid-state method. Stoichiometric amounts of starting materials, RbX and AgX, were weighed precisely and ground for 30 minutes for homogeneous mixing inside a nitrogen-filled glove box. The grounded mixtures were pressed into pellets, then sealed under approximately 5 mTorr vacuum. The pellets of Rb_2AgCl_3, Rb_2AgBr_3, and Rb_2AgI_3 were annealed at 260 °C, 268 °C and 260 °C for 60 hours, 60 hours, and 96 hours, respectively. This procedure was repeated by regrinding the collected pellets, re-pelletizing, and annealing under the same conditions to ensure sample homogeneity and total consumption of reactants. To test the sample-to-sample variation in the optical properties, Rb_2AgI_3 samples with a short annealing time of 12 hours were also prepared.

Cs_2AgX_3 (X = Br, I) Synthesis: Cs_2AgX_3 (X = Br, I) were also synthesized using solid-state techniques. Stoichiometric 2:1 ratios of CsX and AgX were weighed precisely and ground for 30 minutes for homogeneous mixing inside a nitrogen-filled glove box, pressed into pellets, and sealed under approximately 5mTorr vacuum. The Cs_2AgBr_3 and Cs_2AgI_3 pellets were annealed at 260°C and 240°C for 160 hours and 80 hours, respectively, and cooled to room temperature over 12 hours. The obtained samples were then re-ground and pelletized again for a repeated annealing to improve the sample homogeneity and purity.

Ink preparation: To prepare luminescent inks, 2 g of polymethyl methacrylate (PMMA) was added into 5 ml of toluene and stirred at room temperature until PMMA completely dissolved. Then, as-synthesized A_2AgX_3 (R= Rb, Cs, X= Cl, Br, I) polycrystalline powder samples (200 mg) were dispersed in this solution and stirred overnight, followed by sonication for 1 hour. Finally, A_2AgX_3 (R= Rb, Cs, X= Cl, Br, I) based luminescent inks were used for writing a security code for anti-counterfeiting and printing latent fingerprints.

Powder X-ray Diffraction (PXRD): Powder X-ray powder diffraction (PXRD) measurements were taken on a Rigaku Miniflex600 equipped with a D/tex detector and a Rigaku Ultima IV diffractometer, both with a Ni-filtered Cu-Kα radiation source. Data were collected at room temperature in the 3 − 90° (2θ) range, with a step size of 0.02°. For evaluating materials stability, periodic PXRD experiments were taken on powder samples of A_2AgX_3 left in the dark under ambient air conditions at 19.7 °C.

Thermogravimetry and Differential Scanning Calorimetry (TGA/DSC): The thermal stability of polycrystalline powders of A_2AgX_3 (R= Rb, Cs, X= Cl, Br, I) was examined through thermogravimetric analysis and differential scanning calorimetry (TGA/DSC) measurements using a TA Instruments SDT 650 thermal analyzer system. The samples were heated from 25 to 450 °C with a heating rate of 5 °C/min under an inert flow of dry nitrogen gas at a rate of 100 mL/min.

Optical Measurements: Optical properties of polycrystalline powders of A_2AgX_3 were studied using a Jobin Yvon Fluorolog-3 spectrofluorometer (Horiba) equipped with a Xenon lamp (450 W) and Quanta-φ integrating sphere. For each sample, photoluminescence emission (PL), photoluminescence excitation (PLE), and photoluminescence quantum yield (PLQY) measurements were performed from 270 to 750 nm. Time-resolved photoluminescence (TRPL) measurements were taken using a Time-Correlated Single Photon Counting (TCSPC) system that includes a DeltaHub DH-HT high throughput TCSPC controller and NanoLED NL-C2 pulsed

diode controller. For TRPL measurements, a 299 nm NanoLED diode with a <1.2 ns pulse duration was used as an excitation source. In order to fit the data, the following equations were used:

$$I(t) = \sum_{i}^{n} \alpha_i \exp\left(\frac{-t}{\tau_i}\right)$$

$$\alpha_1 = \frac{B_1}{(B_1 + B_2)} \qquad \alpha_2 = \frac{B_2}{(B_1 + B_2)}$$

Fitting parameters are available in Table S1.

Quantum yield is determined by:

$$Quantum\ Yield = \left(\frac{Em_s - Em_b}{Ex_b - Ex_s}\right) \text{x} 100$$

Ex_s and Ex_b are the integrated excitation profiles of the sample, and the blank and Em_s and Em_b are the integrated emission profiles of the sample and blank, respectively. An Area Balance Factor is applied in the FluorEssence software, which accounts for changes in integration times between excitation and emission scans and the use of neutral density filters.

Microscopy: A Thermo Quattro S field-emission environmental Scanning Electron Microscope (FE-ESEM) was utilized to obtain the SEM images. The aliquots of the inks were placed on top of clean silicon plate and images were collected using the back-scattered detector.

Computational Methods: Our calculations were based on density functional theory (DFT) as implemented in the VASP code.[54] The kinetic energy cutoff of the plane-wave basis is 262 eV. The projector augmented wave method was used to describe the interaction between ions and electrons.[55] The lattice parameters were fixed at the experimentally measured values while the atomic positions were optimized until the force on each atom is less than 0.02 eV/Å. The electronic band structure and density of states (DOS) were calculated using Perdew-Burke-Ernzerhof (PBE) exchange-correlation functional[56], and the band gap was further corrected using the hybrid PBE0 functional.[57]

The optimized ground- and excited-state structures [including the structures of self-trapped excitons (STE) and defect-bound excitons] were obtained by using the hybrid PBE0 functional,[57] which has 25% non-local Fock exchange. The occupation numbers of the electron- and hole-occupied eigenlevels are fixed [Δ self-consistent field (ΔSCF) method[58-60]] for the total energy calculation of an exciton and throughout the entire excited-state structural relaxation process. Following the Franck-Condon principle, the excitation and emission energies of an exciton were calculated by taking the energy difference between the excited and the ground state energies using the relaxed ground-state and excited-state structures, respectively.

Supporting Information

TRPL fitting data, computational band gaps, PXRD patterns, TGA/DSC data, excitation-dependent PL, emission-dependent PL, photostability plots, luminescent ink images, and ESEM images.

Author Contributions

The manuscript was written through the contributions of all authors. All authors have approved the final version of the manuscript. P.K., T.C., and H.F., prepared the samples. P.K., T.C., H. F. and M. S. performed PXRD, TGA/DSC measurements, performed and analyzed the optical measurements, M-H.D. Carried out the theoretical calculations, and B.S. conceived and supervised the work.

Acknowledgments

This work was supported by the University of Oklahoma (OU) startup funds and funds provided by the National Science Foundation (DMR-2045490). M. H. Du was supported by the U. S. Department of Energy, Office of Science, Basic Energy Sciences, Materials Sciences, and Engineering Division. We thank Dr. A. S. Madden for his assistance with PXRD measurements.

Isaiah W. Gilley and Timothy M. McWhorter are acknowledged for their assistance in material preparation.

Conflicts of Interest

The authors declare no competing financial interest.

Keywords

Halide perovskites, photoluminescence, high-efficiency light emission, silver(I) halides, copper(I) halides, anti-counterfeiting, fingerprint detection

References

1. Green, M. A.; Ho-Baillie, A.; Snaith, H. J., The emergence of perovskite solar cells. *Nature Photonics* **2014,** *8* (7), 506-514.
2. Yang, Z.; Gao, M.; Wu, W.; Yang, X.; Sun, X. W.; Zhang, J.; Wang, H.-C.; Liu, R.-S.; Han, C.-Y.; Yang, H.; Li, W., Recent advances in quantum dot-based light-emitting devices: Challenges and possible solutions. *Materials Today* **2019,** *24*, 69-93.
3. Wei, Y.; Cheng, Z.; Lin, J., An overview on enhancing the stability of lead halide perovskite quantum dots and their applications in phosphor-converted LEDs. *Chemical Society Reviews* **2019,** *48* (1), 310-350.
4. Cai, M.; Wu, Y.; Chen, H.; Yang, X.; Qiang, Y.; Han, L., Cost-Performance Analysis of Perovskite Solar Modules. *Advanced Science* **2017,** *4* (1), 1600269.
5. Li, C. H. A.; Zhou, Z.; Vashishtha, P.; Halpert, J. E., The Future Is Blue (LEDs): Why Chemistry Is the Key to Perovskite Displays. *Chemistry of Materials* **2019,** *31* (16), 6003-6032.
6. Ono, L. K.; Qi, Y.; Liu, S., Progress toward Stable Lead Halide Perovskite Solar Cells. *Joule* **2018,** *2* (10), 1961-1990.
7. Creason, T. D.; Yangui, A.; Roccanova, R.; Strom, A.; Du, M.-H.; Saparov, B., Rb2CuX3 (X = Cl, Br): 1D All-Inorganic Copper Halides with Ultrabright Blue Emission and Up-Conversion Photoluminescence. *Advanced Optical Materials* **2020,** *8* (2), 1901338.
8. Sum, T. C.; Mathews, N., Advancements in perovskite solar cells: photophysics behind the photovoltaics. *Energy & Environmental Science* **2014,** *7* (8), 2518-2534.
9. Roccanova, R.; Houck, M.; Yangui, A.; Han, D.; Shi, H.; Wu, Y.; Glatzhofer, D. T.; Powell, D. R.; Chen, S.; Fourati, H.; Lusson, A.; Boukheddaden, K.; Du, M.-H.; Saparov, B., Broadband Emission in Hybrid Organic–Inorganic Halides of Group 12 Metals. *ACS Omega* **2018,** *3* (12), 18791-18802.
10. Wu, M.; Haji Ladi, N.; Yi, Z.; Li, H.; Shen, Y.; Wang, M., Stability Issue of Perovskite Solar Cells under Real-World Operating Conditions. *Energy Technol. (Weinheim, Ger.)* **2020,** *8* (4), 1900744.
11. Bi, C.; Wang, S.; Kershaw, S. V.; Zheng, K.; Pullerits, T.; Gaponenko, S.; Tian, J.; Rogach, A. L., Spontaneous Self-Assembly of Cesium Lead Halide Perovskite Nanoplatelets into Cuboid Crystals with High Intensity Blue Emission. *Adv. Sci.* **2019,** *6* (13), 1900462.
12. Dai, X.; Deng, Y.; Peng, X.; Jin, Y., Quantum-Dot Light-Emitting Diodes for Large-Area Displays: Towards the Dawn of Commercialization. *Advanced Materials* **2017,** *29* (14), 1607022.
13. Huang, H.; Polavarapu, L.; Sichert, J. A.; Susha, A. S.; Urban, A. S.; Rogach, A. L., Colloidal lead halide perovskite nanocrystals: synthesis, optical properties and applications. *Npg Asia Materials* **2016,** *8*, e328.
14. Protesescu, L.; Yakunin, S.; Bodnarchuk, M. I.; Krieg, F.; Caputo, R.; Hendon, C. H.; Yang, R. X.; Walsh, A.; Kovalenko, M. V., Nanocrystals of Cesium Lead Halide Perovskites ($CsPbX_3$, X = Cl, Br, and I): Novel Optoelectronic Materials Showing Bright Emission with Wide Color Gamut. *Nano Lett.* **2015,** *15* (6), 3692-3696.
15. Lu, S.; Zhou, Q.; Ouyang, Y.; Guo, Y.; Li, Q.; Wang, J., Accelerated discovery of stable lead-free hybrid organic-inorganic perovskites via machine learning. *Nature Communications* **2018,** *9* (1), 3405.
16. Mo, X.; Li, T.; Huang, F.; Li, Z.; Zhou, Y.; Lin, T.; Ouyang, Y.; Tao, X.; Pan, C., Highly-efficient all-inorganic lead-free 1D CsCu2I3 single crystal for white-light emitting diodes and UV photodetection. *Nano Energy* **2020**, 105570.

17. Yang, B.; Yin, L.; Niu, G.; Yuan, J.-H.; Xue, K.-H.; Tan, Z.; Miao, X.-S.; Niu, M.; Du, X.; Song, H.; Lifshitz, E.; Tang, J., Lead-Free Halide Rb2CuBr3 as Sensitive X-Ray Scintillator. *Advanced Materials* **2019,** *31* (44), 1904711.
18. Creason, T. D.; McWhorter, T. M.; Bell, Z.; Du, M.-H.; Saparov, B., K2CuX3 (X = Cl, Br): All-Inorganic Lead-Free Blue Emitters with Near-Unity Photoluminescence Quantum Yield. *Chemistry of Materials* **2020,** *32* (14), 6197-6205.
19. Gao, W.; Yin, L.; Yuan, J.-H.; Xue, K.-H.; Niu, G.; Yang, B.; Hu, Q.; Liu, X.; Tang, J., Lead-free violet-emitting K2CuCl3 single crystal with high photoluminescence quantum yield. *Organic Electronics* **2020,** *86*, 105903.
20. Sharma, M.; Yangui, A.; Whiteside, V. R.; Sellers, I. R.; Han, D.; Chen, S.; Du, M.-H.; Saparov, B., Rb4Ag2BiBr9: A Lead-Free Visible Light Absorbing Halide Semiconductor with Improved Stability. *Inorg. Chem.* **2019,** *58* (7), 4446–4455.
21. Luo, J.; Hu, M.; Niu, G.; Tang, J., Lead-Free Halide Perovskites and Perovskite Variants as Phosphors toward Light-Emitting Applications. *ACS Applied Materials & Interfaces* **2019,** *11* (35), 31575-31584.
22. Li, Y.; Yang, K., High-throughput computational design of organic–inorganic hybrid halide semiconductors beyond perovskites for optoelectronics. *Energy & Environmental Science* **2019,** *12* (7), 2233-2243.
23. Jun, T.; Sim, K.; Iimura, S.; Sasase, M.; Kamioka, H.; Kim, J.; Hosono, H., Lead-Free Highly Efficient Blue-Emitting Cs3Cu2I5 with 0D Electronic Structure. *Adv. Mater.* **2018,** *30* (43), 1804547.
24. Sun, J.; Yang, J.; Lee, J. I.; Cho, J. H.; Kang, M. S., Lead-Free Perovskite Nanocrystals for Light-Emitting Devices. *The Journal of Physical Chemistry Letters* **2018,** *9* (7), 1573-1583.
25. Chakraborty, S.; Xie, W.; Mathews, N.; Sherburne, M.; Ahuja, R.; Asta, M.; Mhaisalkar, S. G., Rational Design: A High-Throughput Computational Screening and Experimental Validation Methodology for Lead-Free and Emergent Hybrid Perovskites. *ACS Energy Letters* **2017,** *2* (4), 837-845.
26. Saparov, B.; Sun, J.-P.; Meng, W.; Xiao, Z.; Duan, H.-S.; Gunawan, O.; Shin, D.; Hill, I. G.; Yan, Y.; Mitzi, D. B., Thin-Film Deposition and Characterization of a Sn-Deficient Perovskite Derivative Cs2SnI6. *Chem. Mater.* **2016,** *28* (7), 2315-2322.
27. Morad, V.; Shynkarenko, Y.; Yakunin, S.; Brumberg, A.; Schaller, R. D.; Kovalenko, M. V., Disphenoidal Zero-Dimensional Lead, Tin, and Germanium Halides: Highly Emissive Singlet and Triplet Self-Trapped Excitons and X-ray Scintillation. *J. Am. Chem. Soc.* **2019**.
28. Peng, H.; Yao, S.; Guo, Y.; Zhi, R.; Wang, X.; Ge, F.; Tian, Y.; Wang, J.; Zou, B., Highly Efficient Self-Trapped Exciton Emission of a (MA)4Cu2Br6 Single Crystal. *The Journal of Physical Chemistry Letters* **2020,** *11* (12), 4703-4710.
29. Roccanova, R.; Yangui, A.; Nhalil, H.; Shi, H.; Du, M.-H.; Saparov, B., Near-Unity Photoluminescence Quantum Yield in Blue-Emitting $Cs_3Cu_2Br_{5-x}I_x$ ($0 \leq x \leq 5$). *ACS Appl. Electron. Mater.* **2019,** *1* (3), 269-274.
30. Roccanova, R.; Yangui, A.; Seo, G.; Creason, T. D.; Wu, Y.; Kim, D. Y.; Du, M.-H.; Saparov, B., Bright Luminescence from Nontoxic CsCu2X3 (X = Cl, Br, I). *ACS Materials Lett.* **2019,** *1*, 459-465.
31. Cowley, A. Novel ultra-violet/blue optoelectronic materials and devices based on copper halides (CuHa). Dublin City University, 2012.
32. Dou, L.; Lai, M.; Kley, C. S.; Yang, Y.; Bischak, C. G.; Zhang, D.; Eaton, S. W.; Ginsberg, N. S.; Yang, P., Spatially resolved multicolor CsPbX₃ nanowire

heterojunctions via anion exchange. *Proceedings of the National Academy of Sciences* **2017**, 201703860.
33. Zhang, F.; Zhong, H.; Chen, C.; Wu, X.-g.; Hu, X.; Huang, H.; Han, J.; Zou, B.; Dong, Y., Brightly Luminescent and Color-Tunable Colloidal CH3NH3PbX3 (X = Br, I, Cl) Quantum Dots: Potential Alternatives for Display Technology. *ACS Nano* **2015,** *9* (4), 4533-4542.
34. Du, M.-H., Emission Trend of Multiple Self-Trapped Excitons in Luminescent 1D Copper Halides. *ACS Energy Letters* **2020,** *5* (2), 464-469.
35. Zhao, X.; Niu, G.; Zhu, J.; Yang, B.; Yuan, J.-H.; Li, S.; Gao, W.; Hu, Q.; Yin, L.; Xue, K.-H.; Lifshitz, E.; Miao, X.; Tang, J., All-Inorganic Copper Halide as Stable and Self-Absorption Free X-Ray Scintillator. *The Journal of Physical Chemistry Letters* **2020,** *11* (5), 1873-1880.
36. Seo, G.; Jung, H.; Creason, T. D.; Yeddu, V.; Bamidele, M.; Echeverria, E.; Lee, J.; McIlroy, D.; Saparov, B.; Kim, D. Y., Lead-Free Halide Light-Emitting Diodes with External Quantum Efficiency Exceeding 7% Using Host–Dopant Strategy. *ACS Energy Letters* **2021,** *6* (7), 2584-2593.
37. Ding, M.; Dong, B.; Lu, Y.; Yang, X.; Yuan, Y.; Bai, W.; Wu, S.; Ji, Z.; Lu, C.; Zhang, K.; Zeng, H., Energy Manipulation in Lanthanide-Doped Core-Shell Nanoparticles for Tunable Dual-Mode Luminescence toward Advanced Anti-Counterfeiting. *Adv Mater* **2020,** *32* (45), e2002121.
38. Liu, Y.; Han, F.; Li, F.; Zhao, Y.; Chen, M.; Xu, Z.; Zheng, X.; Hu, H.; Yao, J.; Guo, T.; Lin, W.; Zheng, Y.; You, B.; Liu, P.; Li, Y.; Qian, L., Inkjet-printed unclonable quantum dot fluorescent anti-counterfeiting labels with artificial intelligence authentication. *Nature Communications* **2019,** *10* (1), 2409.
39. Hull, S.; Berastegui, P., Crystal structures and ionic conductivities of ternary derivatives of the silver and copper monohalides—II: ordered phases within the (AgX)x–(MX)1−x and (CuX)x–(MX)1−x (M=K, Rb and Cs; X=Cl, Br and I) systems. *J. Solid State Chem.* **2004,** *177* (9), 3156-3173.
40. Martins, D. T. A.-A. In *Compact ion-source based on superionic rubidium silver iodide (RbAg4I5) solid electrolyte*, 2013.
41. Bradley, J. N.; Greene, P. D., Solids with high ionic conductivity in group 1 halide systems. *Transactions of the Faraday Society* **1967,** *63* (0), 424-430.
42. Li, S.; Luo, J.; Liu, J.; Tang, J., Self-Trapped Excitons in All-Inorganic Halide Perovskites: Fundamentals, Status, and Potential Applications. *J. Phys. Chem. Lett.* **2019**, 1999-2007.
43. Zhang, M.; Wang, X.; Yang, B.; Zhu, J.; Niu, G.; Wu, H.; Yin, L.; Du, X.; Niu, M.; Ge, Y.; Xie, Q.; Yan, Y.; Tang, J., Metal Halide Scintillators with Fast and Self-Absorption-Free Defect-Bound Excitonic Radioluminescence for Dynamic X-Ray Imaging. *Advanced Functional Materials* **2021,** *31* (9), 2007921.
44. Zhang, Z.; Zhao, R.; Teng, S.; Huang, K.; Zhang, L.; Wang, D.; Yang, W.; Xie, R.; Pradhan, N., Color Tunable Self-Trapped Emissions from Lead-Free All Inorganic IA-IB Bimetallic Halides Cs-Ag-X (X = Cl, Br, I). *Small* **2020,** *16* (44), 2004272.
45. Bill, H.; Hollingsworth, G. J.; McClure, D. S.; Moine, B.; Pedrini, C., Optical spectroscopy of the Ag+ ion in NaF: Experimental results and analysis of manifestations of the Jahn–Teller effect. *The Journal of Chemical Physics* **1998,** *109* (17), 7328-7337.

46. Yanagida, T., Inorganic scintillating materials and scintillation detectors. *Proc Jpn Acad Ser B Phys Biol Sci* **2018,** *94* (2), 75-97.
47. Nikl, M.; Yoshikawa, A., Recent R&D Trends in Inorganic Single-Crystal Scintillator Materials for Radiation Detection. *Advanced Optical Materials* **2015,** *3* (4), 463-481.
48. Bhaumik, S.; Bruno, A.; Mhaisalkar, S., Broadband emission from zero-dimensional Cs4PbI6 perovskite nanocrystals. *RSC Advances* **2020,** *10* (23), 13431-13436.
49. Baranowski, M.; Plochocka, P., Excitons in Metal-Halide Perovskites. *Advanced Energy Materials* **2020,** *10* (26).
50. Du, M.-H., Microscopic origin of multiple exciton emission in low-dimensional lead halide perovskites. *The Journal of Chemical Physics* **2019,** *151* (18), 181101.
51. Awano, T.; Matsuyama, T., Self-trapped holes in ammonium silver bromide crystal. *Nuclear Instruments & Methods in Physics Research Section B-beam Interactions With Materials and Atoms - NUCL INSTRUM METH PHYS RES B* **1994,** *91*, 227-229.
52. Creason, T. D.; Fattal, H.; Gilley, I. W.; McWhorter, T. M.; Du, M.-H.; Saparov, B., (NH4)2AgX3 (X = Br, I): 1D Silver Halides with Broadband White Light Emission and Improved Stability. *ACS Materials Au* **2021**.
53. Bramble, S. K.; Creer, K. E.; Gui Qiang, W.; Sheard, B., Ultraviolet luminescence from latent fingerprints. *Forensic Science International* **1993,** *59* (1), 3-14.
54. Kresse, G.; Furthmüller, J., Efficiency of ab-initio total energy calculations for metals and semiconductors using a plane-wave basis set. *Computational Materials Science* **1996,** *6* (1), 15-50.
55. Kresse, G.; Joubert, D., From ultrasoft pseudopotentials to the projector augmented-wave method. *Physical Review B* **1999,** *59* (3), 1758.
56. Perdew, J. P.; Burke, K.; Ernzerhof, M., Generalized gradient approximation made simple. *Physical review letters* **1996,** *77* (18), 3865.
57. Perdew, J. P.; Emzerhof, M.; Burke, K., Rationale for mixing exact exchange with density functional approximations. *Journal of Chemical Physics* **1996,** *105* (22), 9982-9985.
58. Jones, R. O.; Gunnarsson, O., The density functional formalism, its applications and prospects. *Reviews of Modern Physics* **1989,** *61* (3), 689-746.
59. Görling, A., Density-functional theory beyond the Hohenberg-Kohn theorem. *Physical Review A* **1999,** *59* (5), 3359-3374.
60. Hellman, A.; Razaznejad, B.; Lundqvist, B. I., Potential-energy surfaces for excited states in extended systems. *The Journal of Chemical Physics* **2004,** *120* (10), 4593-4602.

TOC

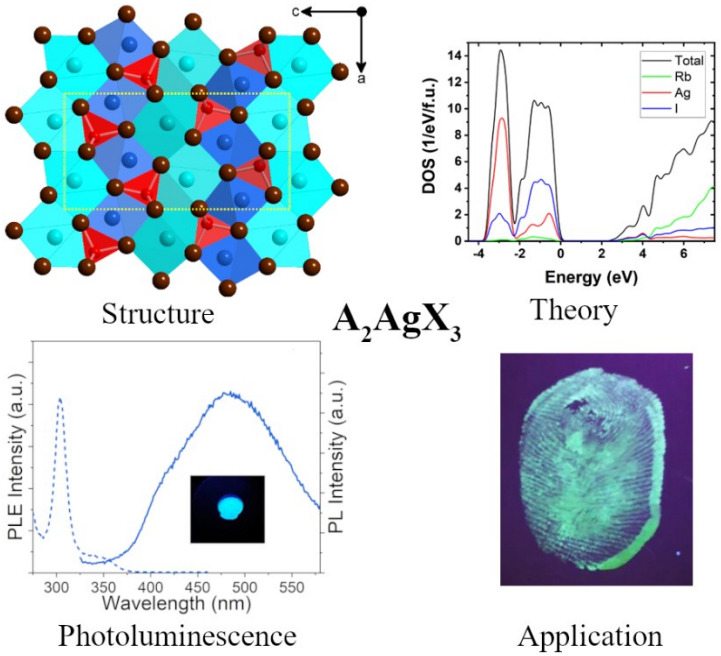

Photoluminescent copper(I) halides have recently emerged as exciting non-toxic and earth-abundant alternatives to lead halide perovskites, however, these suffer from the lack of tunability of their photoemission properties and poor stability in ambient air. Here, we report silver(I) halides with tunable light emission properties and much improved stability, which enables their use in anti-counterfeiting applications.